# Copper-perovskite interfacial engineering to boost deNOx activity

Asghar Mohammadi [a], Clivia Hejny [b], Volker Kahlenberg [b], Josef M. Gallmetzer [c], Felix R.S. Purtscher [c], Thomas S. Hofer [c], Marc Heggen [d], Maged F. Bekheet [e], Simon Penner [a],*

[a] *Institute of Physical Chemistry, University of Innsbruck, Innrain 52c, A-6020 Innsbruck, Austria*
[b] *Institute for Mineralogy and Petrography, University of Innsbruck, Innrain 52d, A-6020 Innsbruck, Austria*
[c] *Institute of Genreal, Inorganic and Theoretical Chemistry, Innrain 80-82, University of Innsbruck, A-6020 Innsbruck, Austria*
[d] *Ernst Ruska-Centre for Microscopy and Spectroscopy with Electrons, Forschungszentrum Jülich GmbH, Leo-Brandt-Str. 1, D-52428 Jülich, Germany*
[e] *Technische Universität Berlin, Faculty III Process Sciences, Institute of Materials Science and Technology, Chair of Advanced Ceramic Materials, Straße Des 17. Juni 135, 10623 Berlin, Germany*

ARTICLE INFO

ABSTRACT

By adjusting the Cu doping level and calcination temperature during synthesis of a series of noble metal-free lanthanum copper manganite perovskites $LaCu_xMn_{1-x}O_3$, we show the importance of tuning the redox chemistry for optimum steering of the catalytic activity and $N_2$ selectivity in the catalytic reduction of NO by CO. A prerequisite is the in situ formation of an extended copper-perovskite phase boundary. The associated improvement of redox and surface properties by Cu addition leads to an optimized balance of the reduction of the catalyst in the NO+CO reaction mixture. The creation of oxygen vacancies improves the reaction kinetics and initiates the NO dissociation. Strongly dependent on the calcination temperature, the Cu/Mn ratio, the reducing agent, as well as the reaction temperature as parameters for Cu-perovskite interfacial control, surface reduction can induce partial copper exsolution, significant perovskite reduction, agglomeration of exsolved Cu particles and eventual decomposition of the catalyst structure. We show that increasing the amount of initial copper incorporated into the perovskite structure can beneficially extend the phase boundary, but exceeding the amount of copper leads to increased sintering of the copper particles at the expense of catalyst activity, especially in repeated catalytic cycles. Increasing the calcination temperature, in addition to the initial sintering of the catalyst and shifting the reaction onset temperature to higher temperatures in the first cycle, improves the reduction resistance of the catalyst. Consequently, in order to form a higher amount of phase boundary-bound active sites, stronger reducing conditions than provided by the NO+CO reaction mixture are needed. This effect can be counterbalanced by using stronger reduction agents prior to performing subsequent catalytic cycles by inducing the exsolution process.

## 1. Introduction

The reduction of NO by CO (Eq. (1) is an important reaction in denitrification processes of exhaust gas from combustion engines [1].

$$2NO + 2CO \rightleftarrows N_2 + 2CO_2 \tag{1}$$

$$2NO + CO \rightleftarrows N_2O + CO_2 \tag{2}$$
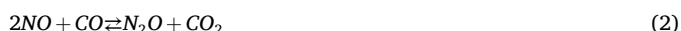
An important reaction intermediate, arising from the partial reduction of NO (eq. (2), is $N_2O$, a highly stable greenhouse gas with a global warming potential exceeding $CO_2$ by a factor of almost 300 [2,3]. The model reaction (eq. (3)

$$N_2O + CO \rightleftarrows N_2 + CO_2 \tag{3}$$

describes the reduction of $N_2O$ by CO. From eq. (3) it is clear that in order to maximize the $N_2$ selectivity, it is imperative to use catalyst materials that provide fast onward reductive degradation of $N_2O$ or limit its intermediate production by increasing the rate of the first reaction [4].

Supported noble metals (e.g. platinum group metals such as Rh, Pd or Pt) have been intensively studied, but will inevitably be replaced by other material types to economize their use. [5–7]. A very promising class of complex oxide materials encompasses $ABO_3$ perovskites. A and B are typically bi- or tri-valent cations such as $La^{3+}$, earth alkaline cations

(for A), or transition metals cations (for B). A promising property of such perovskites specifically for the efficient reduction of NO by CO is the ability to activate NO on oxygen-deficient sites, which can also be introduced by substitution of ions within the perovskite structure at the A- or B-site [8–16]. The reaction of CO with the replenished oxygen vacancy to $CO_2$ closes the catalytic cycle in a Mars–van–Krevelen–type reaction. With respect to the fast reaction/decomposition of $N_2O$, copper-containing perovskites have shown promising behavior, despite the general limitations of poor sinter and oxidation stability, especially in oxidizing environments [17–22]. A concept combining both beneficial properties – NO activation at oxygen defects and high $N_2O$ reactivity – and to some extent also to overcome the restrictions discussed above, is the controlled exsolution of metal particles from the perovskite structure and the associated formation of a metal-perovskite interface [23–26]. Exsolution, which usually occurs due to the chemical reduction of the host oxide, is a promising method for the self-production of catalytic nanoparticles decorating the oxide surface [23,27]. Compared to deposited or infiltrated nanoparticles, exsolved nanoparticles can anchor to the host oxide, increasing their resistance to agglomeration and poisoning (i.e., coking) [28–30]. We have recently shown for Cu-doped lanthanum manganite perovskites at selected Cu/Mn ratios that controlled exsolution of Cu particles allows the exact tuning of the de-nitrification activity and that the resulting Cu-perovskite interface is, in principle, capable of entirely replacing noble metals [31]. One obstacle, however, remains: exsolution of metal particles is strongly dependent on the doping level of the perovskites, i.e., the perovskite composition. This, in turn, affects both the structure and the stability of the perovskite. The aforementioned Cu-doped lanthanum manganite perovskite serves as an illustrative example in this respect: a single phase-pure lanthanum copper manganite structure $LaCu_xMn_{1-x}O_3$ is only observed for compositions $x \leq 0.5$. Higher Cu contents inevitably lead to excess Cu phases ($La_2CuO_4$ and/or $CuO$) and to strongly altered exsolution behavior and associated Cu-perovskite interfacial dimensions. This necessarily goes along with altered Cu particle sizes and reactivity of the Cu-perovskite interface. Specifically, a short literature review of Cu-doped lanthanum manganite perovskite structures exploited for a variety of reactions, e.g., CO oxidation, NO reduction by CO or NO removal tentatively reveals phase pure $LaCu_xMn_{1-x}O_3$ in the compositional region $0 \leq x \leq 0.6$ for selected calcination temperatures between 600 °C and 750 °C.

In addition to important characteristics of exsolved nanoparticles such as composition, size and density, an equally important parameter in the exsolved system concerns the host oxide's surface properties after exsolution. This issue becomes important in systems, where reactive zones are not necessarily limited to metallic particles, but can also be extended to the oxide surface, similar to our perovskite oxides in this work. According to literature, this issue has already been addressed in several works in different catalytic systems [32–36].

In due course, as the copper-perovskite interface in principle has been shown to economize the use of noble metals, we strive to systematically explore the Cu/Mn composition space in $LaCu_xMn_{1-x}O_3$ to clarify the structural prerequisites of enhanced Cu exsolution and the according catalytic properties. We follow a two-pronged approach here: First, by systematic variation of the Cu/Mn ratio in $LaCu_xMn_{1-x}O_3$ between $x = 0$ and $x = 1$ and the calcination temperature of the perovskite during sol–gel synthesis, we will show how the calcination temperature affects the incorporation of Cu into the $LaMnO_3$ host structure at given Cu/Mn ratios and eventually, phase-pure $LaCu_xMn_{1-x}O_3$ phases may result even for compositions $x > 0.5$. If successful, controlled Cu exsolution from the lattice will eventually yield a higher Cu content on the surface, boosting the de-nitrification activity. Secondly, the ultimate goal is to correlate the effect of calcination temperature for given Cu/Mn ratios to catalytic activity and establish unambiguous structure–activity relationships to identify the best-working Cu-perovskite interface. This problem will be approached mainly experimentally (i.e., by Rietveld analysis of experimentally obtained X-ray diffraction patterns), but

supported by additional theoretical modeling of various Cu-doped lanthanum manganite structures.

## 2. Experimental

### 2.1. Synthesis of materials

A sol–gel synthesis approach using the metal nitrate precursor materials ($La(NO_3)_3 \cdot 6H_2O$, $Mn(NO_3)_2 \cdot 4H_2O$, $Cu(NO_3)_2 \cdot 5H_2O$) was followed for the preparation of the lanthanum copper manganite samples with different nominal Cu/Mn ratio. Details of the synthesis routine are outlined in Ref. [37]. A final calcination step for 5 h at 600 °C to 1000 °C (for different samples) yielded the starting materials, which were characterized by ex-situ PXRD to verify successful synthesis. Table 1 gives an overview of the nominal compositions and the acronyms used. The numbers after the LCM acronym indicate the B site ratio of Cu and Mn cations, and the number after the dash indicates the calcination temperature in °C. For example, "LCM37-700C" refers to $LaCu_{0.3}Mn_{0.7}O_3$ calcined at 700 °C.

### 2.2. Structural characterization

Powder X-ray diffraction patterns of the initial samples and after the NO-CO reaction were recorded with a Rigaku SmartLab-SE diffractometer in focusing beam setting and reflections mode on a θ/θ goniometer and Co-Kα radiation, ($\lambda = 1.78900$ Å) using a D/teX Ultra 250 compound silicon strip 1D-detector. Patterns were recorded with an incident slit of 0.5° in a range from 5° to 80° 2θ with a step width of 0.005° and a speed of 0.5° min$^{-1}$. The software SmartLab Studio-II (Rigaku Corporation, 2014) was used for diffractometer control and phase assignment using the PDF-4+ (International Centre for Diffraction Data 2023) database. Rietveld analysis was performed using the HighScore Plus software. Peaks were fitted by functions with corresponding Gauss and Lorentz parts.

Elemental analysis for lanthanum (La), copper (Cu) and manganese (Mn) were performed with inductively coupled plasma optical emission spectroscopy (ICP-OES) by using a Horiba Scientific ICP Ultima2 (Horiba, Kyoto, Japan). Prior to analysis, powder samples were dissolved in an aqueous suspension of $HNO_3$ and HF acid mixture at 200 °C for 5 h in a Teflon-lined autoclave.

BET-based specific surface areas were measured by nitrogen adsorption, using a Quanta-Chrome Nova 2000e surface and pore size analyzer and liquid $N_2$ as adsorbent. Before testing, the samples were degassed at 270 °C *in vacuo* for 1 h.

Structural and morphological characterization for selected catalyst states was further performed by aberration-corrected transmission electron microscopy (TEM) at the Ernst-Ruska Center for microscopy and spectroscopy with electrons at FZ Jülich using a FEI Titan 80–300 STEM microscope operated at 300 kV.

### 2.3. Spectroscopic characterization

X-ray photoelectron spectroscopy (XPS) measurements were performed using a VG ESCALAB apparatus and a monochromated Al-Kα X-ray source (E=1487 eV). XP spectra were collected after initial calcination of the samples and after catalysis at 500 °C for the representative LCM55-700C catalyst. Evaluation of the data was performed using the CasaXPS software. For calculation of the surface ion concentration, relative sensitivity factor (RSF) and electron mean free path corrections have been applied. Detailed information is available in Ref. [4].

### 2.4. Temperature-Programmed reduction profiles

Hydrogen temperature-programmed reduction ($H_2$-TPR) and $O_2$/NO temperature-programmed desorption ($O_2$/NO-TPD) measurements were performed in a setup for volumetric adsorption of gases consisting of a

**Table 1**

Overview of catalyst nominal composition, BET-derived specific surface area (SSA), composition derived from ICP analysis and surface composition by XPS.

| Nominal Composition | Acronyms | SSA /$m^2gr^{-1}$ | Chemical composition based on ICP | Chemical composition based on XPS |
|---|---|---|---|---|
| LaMnO$_3$ | LM-700C | 16.6 | La$_{1.03}$Mn$_{0.97}$O$_{3-\delta}$ | – |
| LaCu$_{0.3}$Mn$_{0.7}$O$_3$ | LCM37-700C | 21.5 | La$_{1.07}$Cu$_{0.29}$Mn$_{0.64}$O$_{3-\delta}$ | La$_{1.65}$Cu$_{0.09}$Mn$_{0.26}$O$_{3-\delta}$ |
| LaCu$_{0.5}$Mn$_{0.5}$O$_3$ | LCM55-700C | 13.6 | La$_{1.07}$Cu$_{0.49}$Mn$_{0.44}$O$_{3-\delta}$ | La$_{1.57}$Cu$_{0.31}$Mn$_{0.12}$O$_{3-\delta}$ |
| LaCu$_{0.7}$Mn$_{0.3}$O$_3$ | LCM73-700C | 15.8 | La$_{1.04}$Cu$_{0.69}$Mn$_{0.26}$O$_{3-\delta}$ | La$_{1.60}$Cu$_{0.33}$Mn$_{0.08}$O$_{3-\delta}$ |
| LaCu$_{0.9}$Mn$_{0.1}$O$_3$ | LCM91-700C | 13.0 | La$_{1.04}$Cu$_{0.88}$Mn$_{0.08}$O$_{3-\delta}$ | – |
| La$_2$CuO$_4$ | LC-700C | 12.0 | La$_{1.04}$Cu$_{0.96}$O$_{3-\delta}$ | – |

quartz tubular reactor (volume 34.5 mL). As for H$_2$-TPR, a defined amount of about 60 mg of the powder sample was fixed by quartz wool in the reactor in a chemically inert environment. Catalysts are pretreated in flowing dry O$_2$ for 1 h at 700 °C and subsequently cooled down in O$_2$ atmosphere. To desorb surface- and physically-adsorbed oxygen, samples are evacuated up to a defined base pressure of 10$^{-6}$ mbar. During H$_2$-TPR a defined (ca. 490 mbar) amount of pre-dried H$_2$ (using a liquid N$_2$ cooling trap) was expanded from a separately calibrated volume (9 mL) into the entire reactor volume. After equilibration of the final reactor pressure, the temperature program was started to measure the H$_2$ uptake up to 700 °C. The temperature program included a heating phase from RT to 700 °C at a rate of 10 °C min$^{-1}$, followed by an isothermal period at 700 °C for 10 min, and finally, a cooling process to room temperature (rate 10 °C min$^{-1}$). Additional information, including the technical information of the setup, test conditions, and method of calculation the H$_2$-uptake, is detailed in refs. [37,38]. A QMS system from Balzers (QMA 125; QME 125–9) was employed for continuous gas analysis during TPD measurements. The relevant gases were detected by their respective molecular ions: N$_2$/CO ($m/z = 28$), NO ($m/z = 30$), O$_2$ ($m/z = 32$), N$_2$O/CO$_2$ ($m/z = 44$), and NO$_2$ ($m/z = 46$).

For the O$_2$-TPD tests, in each experimental sequence about 100 mg of catalyst was tested. After the O$_2$ preatreatment phase the samples are evacuated at room temperature to the base pressure (10$^{-6}$ mbar) and subsequently, heating is started with the same temperature program as for the H$_2$-TPR tests. NO-TPD was conducted directly after the O$_2$-TPD, i. e., after O$_2$-TPD the same samples are exposed to dry NO adsorption at room temperature for 45 min at a defined pressure of 1000 mbar NO. Again, after evacuation at RT and re-evacuating, the temperature ramp for NO-TPD tests is started. The experimental conditions for CO-TPR tests are similar to the catalytic activity test conditions (refer to section 2.6) with the difference that instead of NO, an additional He flow is used to provide a total flow rate of 200 mL min$^{-1}$ (CO: He = 1:99 mL min$^{-1}$).

### 2.5. Diffuse reflectance Fourier-Transform infrared spectroscopic (DRIFT) measurements of NH$_3$ adsorption

NH$_3$ adsorption was conducted on powder samples placed in a heated DRIFT cell (PIKE) equipped with CaF$_2$ windows and mounted on a Agilent Cary 660 FT-IR spectrometer. The as-prepared catalysts were placed in an alumina sample holder (Diffuse IR HC Porous Ceramic cup, 6.0 mm OD, 4.0 mm height, 4.7 mm ID and 2.0 mm depth) and pre-treated at 600 °C in He flow (100 mL min$^{-1}$). A background spectrum (60 scans) was recorded at each desired temperature under He flow during cooling the sample after the pre-treatment phase·NH$_3$ adsorption was carried out at room temperature. The catalyst was exposed to 10000 ppm flowing NH$_3$ in He for 45 min followed by flushing with He (100 mL min$^{-1}$) to remove gas phase NH$_3$ and physically adsorbed species. Kubelka-Munk normalized spectra (30 scans) were collected as a function of adsorption time to monitor the evolution of adsorbed species during the NH$_3$ adsorption and saturation and after subsequent He flushing. For the spectra during heating, corresponding background spectra recorded at the same temperature and He flow, were used.

### 2.6. Catalytic measurements

200 mg of catalyst powder was fixed with quartz wool in a home-made 8 mm (inner diameter) quartz fixed-bed flow reactor setup under atmospheric pressure and a total flow rate of 200 mL min$^{-1}$ (in the absence of O$_2$: CO: NO: He = 1:1:98 mL min$^{-1}$, GHSV=9000 h$^{-1}$). For the experiments with variable NO and O$_2$ concentration, the percentage of the gases was adjusted accordingly and was balanced with He to a total flow rate of 200 mL min$^{-1}$. In each catalytic test, the reactor was heated in a Linn High Therm tube furnace at 2 °C min$^{-1}$ to 500 °C (or 650 °C) followed by an isothermal period at maximum temperature for 10 min. The output gas was directly detected by infrared spectroscopy of the gas phase (Agilent Cary 660 FT-IR). As the outlet line is already connected to a quadrupole mass spectrometer (Balzers QME 125), the NO conversion results are also double-checked with QMS. N$_2$ formation rates were determined by difference from the measured rates of NO conversion (NO$_x$ = NO+NO$_2$ in the presence of O$_2$) and of N$_2$O. For quantification of N$_2$O and NO$_2$, external calibration of IR signals has been done using a known composition of N$_2$O and NO$_2$ in He. To display the catalytic activity as a function of temperature, we use the following equation to calculate the NO (or NO$_x$) conversion:

$$NO_{Conversion} = 100*(1 - \frac{[NO]_{out}}{[NO]_{in}})$$

[NO]$_{out}$ and [NO]$_{in}$ indicate the inlet and outlet concentration of NO, respectively. The conversion of oxygen was obtained from QMS.

The impact of mass transport limitations in the chosen reactor setup has been thoroughly assessed and found to be negligible. For details of the calculation, we refer to our previous work [37].

### 2.7. Computational methods

The LCM, LM and LC system calculations were performed using the solid-state DFT code Crystal23 [39]. The hybrid functional HSEsol [40] was employed in conjunction with the pob-DZVP-rev2 basis set [41] for Cu, Mn, and O, and the pob-DTVP-rev2 basis set [41] for La. The convergence criteria for energy and forces were set to 10$^{-7}$ Hartree and 4.5 10$^{-4}$ Hartree Bohr$^{-1}$, respectively. To compare the structural results to the experimental measurements, X-ray powder diffraction patterns of the structures were generated using RIETAN-FP [42] as part of the VESTA [43] program.

## 3. Results and discussion

### 3.1. Composition-dependent incorporation and exsolution of Cu in the LaCu$_x$Mn$_{1-x}$O$_{3-\delta}$ system: Engineering of the Cu-perovskite interface

Ex-situ PXRD patterns of parent LaMnO$_3$ and the Cu-substituted perovskites calcined in air at 700 °C are shown in Fig. 1. LM-700C crystallizes in a trigonal structure (space group *R-3c* H, ICSD coll. Code: 37317, [45]). LCM37-700C perovskite exhibits an orthorhombic structure (space group *Pbnm*, ICSD coll. Code: 92193, [46]). By increasing the amount of copper to 50 % (LCM55-700C), the orthorhombic structure is still maintained, but further increase of the Cu substitution level for LCM73-700C leads to the crystallization of
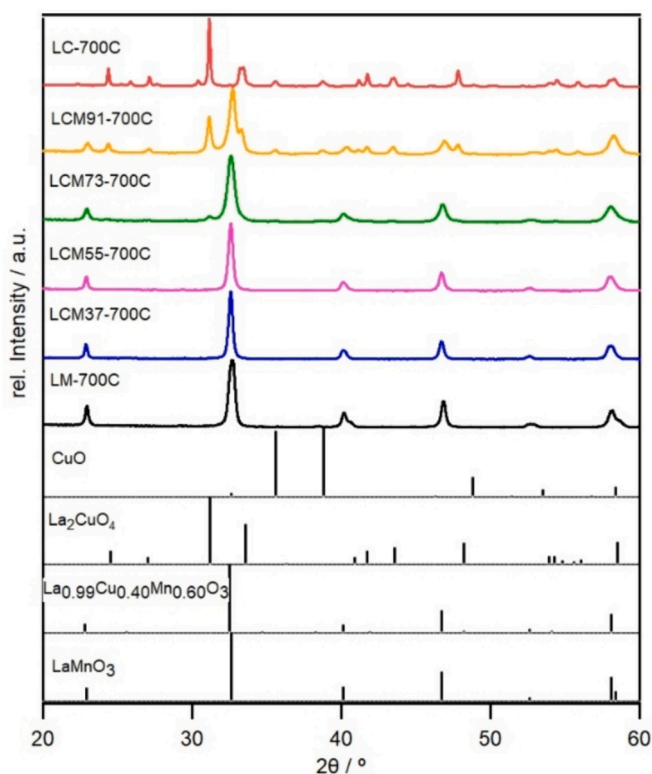
**Fig. 1.** PXRD patterns of the pure and Cu-substituted LM catalysts after initial calcination at T=700 °C in air. References used for structure and phase assignment taken from the ICSD database.

**Table 2**

Cell parameters and cell volumes of the catalysts derived from Rietveld refinement of the experimental PXRD data using CIF files for references from ICSD in comparison with simulated PXRD patterns.

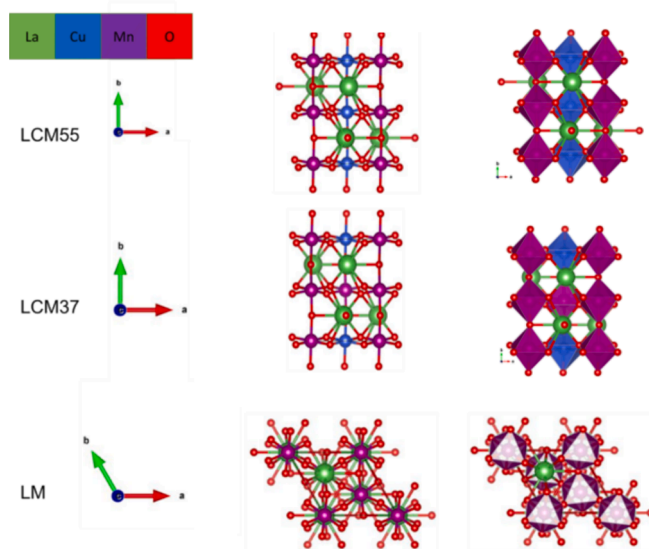| sample | cell parameters | | | cell volume / $\text{Å}^3$ |
|---|---|---|---|---|
| | a / Å | b / Å | c / Å | |
| LM-700C,exp. | 5.5091(5) | 5.5091(5) | 13.349(2) | 350.87 |
| LM,theo. | 5.476 | 5.476 | 13.32 | 345.91 |
| Ref. [45], exp | 5.51053 (18) | 5.51053 (18) | 13.39558 (74) | 352.27 |
| LCM37-700C, exp. | 5.4848(5) | 7.7688(9) | 5.5330(5) | 235.76 |
| LCM1/4,theo. | 5.491 | 7.622 | 5.475 | 229.142 |
| LCM55-700C, exp. | 5.4812(6) | 7.769(1) | 5.5347(6) | 235.68 |
| LCM55,theo. | 5.445 | 7.496 | 5.497 | 224.364 |
| LCM73-700C, exp. | 5.4562(9) | 7.8000(2) | 5.5227(9) | 235.04 |
| LCM3/4,theo. | 5.452 | 7.484 | 5.494 | 224.17 |
| Ref. [44], exp. | 5.4904(3) | 7.7744(5) | 5.5257(3) | 235.86 |



**Fig. 2.** VESTA-drawn crystal structures of LCM samples highlighting the effect of copper substitution in the LCM structure.

additional phases, such as monoclinic CuO and orthorhombic $La_2CuO_4$ spinel structures, respectively. With further increase in the amount of copper, the impurity amount increases, and finally, for LC-700C the contribution of the primary orthorhombic perovskite structure becomes zero.

Different structures of LCM with varying composition were calculated by optimizing them using DFT at HSEsol level of theory [41]. The different LCM compositions were built by substituting Mn with Cu in the orthorhombic unit cell (ICSD 92,193 [46]). To compare the optimized structures with the experimental reference data, PXRD patterns were generated. Fig. S1 shows a comparison of experimental and theoretical diffraction patterns for LCM structures with different compositions based on increased amounts of copper loading. Overall, the theoretically determined diffraction patterns agree well with the experimental results. Slight shifts for the diffraction peaks are observed, resulting from differences between the theoretical single crystal structure and the defective polycrystal structure synthesized under real experimental conditions. Additionally, geometry optimization of the structures formally corresponds to 0 K conditions, which can also be expected to result in slight deviations of the cell parameters.

Cell parameters and cell volumes have been calculated from both the experimental and the simulation results for all 700 °C-calcined catalysts and are presented in Table 2. A slight reduction in unit cell volume by increasing the copper substitution level from LCM37 to LCM73 is evident. Such a reduction in unit cell volume with increasing copper loading level in similar perovskite structures has already been observed by Petrov et al. [44], which can be explained by the smaller ionic radius of $Cu^{2+}$ in comparison with $Mn^{3+}$ (($r(Cu^{2+}) = 54$ pm, $r(Mn^{3+}) = 58$ and 64.5 pm for low spin and high spin, respectively, both ions are 6-fold coordinated).[47].

In Fig. 2, the crystal structures of LCM samples at selected Cu/Mn ratios are shown for illustrative reasons.

In order to investigate the effect of calcination temperature on the

amount of copper that can be accommodated in the perovskite structure, the LCM37, LCM55 and LCM73 catalysts were synthesized at four different calcination temperatures of 600 °C, 700 °C, 850 °C and 1000 °C and the PXRD results are shown in Figs. S2–S4 in the SI. According to Fig. S2, LCM37 forms a pure perovskite even at 600 °C calcination temperature, while LCM55 at this calcination temperature already exhibits some CuO impurity. According to Fig. S3, this CuO impurity is removed by stepwise increasing the calcination temperature to 700 °C. Upon further temperature increase to 1000 °C the pure perovskite phase remains, while the crystallite size increases significantly (Table S1). Also, in the case of LCM73 calcined at 600 °C (Fig. S4), CuO is present. By increasing the calcination temperature to 700 °C and 1000 °C, it is obviously impossible to achieve this pure LCM perovskite structure at this given Cu substitution level. Therefore, the maximum amount of copper that can be incorporated into the perovskite structure is 50 % at the B site, which requires a minimum calcination temperature of 700 °C.

### 3.2. Effect of the composition-dependent Cu-perovskite interface on the structural stability of the perovskite during the NO+CO reaction

PXRD patterns of the LCM catalysts after the NO+CO reaction are

presented in the context of Fig. 3 and S5-S6. Fig. S5 represents the PXRD results of the undoped LM catalyst after two NO+CO reaction cycles at 650 °C. The only structural changes are a partial phase transition of perovskite from initially trigonal to orthorhombic (ICSD coll. Code: 50,336 [48]). No traces of metal oxides (e.g., $MnO_x/LaO_x$) exsolved from the perovskite structure are observed. In contrast, for the Cu-containing catalysts, which initially mainly exhibit an orthorhombic structure, some of the copper exsolves from the perovskite structure as metallic copper after the NO+CO reaction, which is directly dependent on the initial concentration of copper, the calcination temperature, and also the reaction temperature. As it is shown in Fig. 3, Fig. S6 and also based on Rietveld analysis (Table S1), the amount of reaction-induced exsolved copper increases as the reaction temperature and the amount of Cu substitution level increases. The calcination temperature has the opposite effect (Fig. S7), and as the calcination temperature increases, the catalyst becomes more stable under reaction conditions, such that LCM55-1000C shows no PXRD-detectable Cu exsolution during the reaction cycles.

To determine the effect of composition and calcination temperature on the specific surface area (SSA), BET characterization has been carried out (Table 1). In essence, all catalysts exhibit a comparable SSA, and the substitution of Cu at the B site does not have a significant effect on the specific surface of the parent LM perovskite. In the case of LCM55 composition, increasing the calcination temperature from 700 °C to 850 °C and 1000 °C decreases the specific surface area from 13.6 $m^2g^{-1}$ to 10.6 $m^2g^{-1}$ and 9 $m^2g^{-1}$, respectively. As shown in the subsequent catalytic activity and temperature-programmed reduction sections, these properties considerably affect the catalyst's redox and catalytic behavior. As for sintering effects, we anticipate that all other catalysts follow a similar trend for the SSA as a function of calcination temperature.

To verify the nominal bulk composition, the metal content of the perovskites based on ICP analysis is also shown in Table 1 alongside the



**Fig. 3.** PXRD patterns of LCM catalysts after two cycles of NO+CO reaction to highlight the effect of reaction temperature and composition on the structural stability of the catalysts.

surface composition of the catalysts obtained from XPS. The corresponding high-resolution spectra of the La 3d, O 1s, Cu 2p and Mn 2p regions are depicted in Fig. S8, panels A–D, respectively. For all catalysts, a comparison of the nominal composition of the samples with those derived from ICP shows that the content of the elements in the bulk of the samples is close to the nominal ones. According to XPS, the surface of the catalysts is enriched in La and the amount of Cu and Mn almost matches the trend of the nominal composition. Surface enrichment of perovskites with A-site cations is a well-known phenomenon [2]. Compared to fresh LCM55-700C, the surface composition of this catalyst after the NO+CO reaction at 500 °C ($La_{1.59}Cu_{0.28}Mn_{0.13}O_{3-\delta}$) shows a relative decrease in Cu content, which is an important result and in accordance with both PXRD (Fig. 3) and catalytic activity testing (cf. Fig. S12). As will be discussed in detail below, this observation is related to the exsolution and growth of Cu atoms as crystallized metallic Cu particles covering the perovskite surface with further increase in size.

To visualize the morphological and elemental composition dependency on composition, we have conducted electron microscopy experiments for selected materials before and after the NO+CO reaction (Fig. 4). While the manganese-rich LCM materials (Panel A, LCM37) exhibit an agglomerate of rounded grains (size ~200 nm), with progressing Cu enrichment a more fibre-like morphology is obtained (Panel C). This is in agreement with the morphology of benchmark $LaMnO_3$ materials [46,47]. Most notably, we do not observe selective elemental enrichment in any of the initial samples, as evidenced in the EDX maps for LCM55 and LCM73. On the contrary, the structural stability is clearly dependent on the Cu content: while LCM55 does not show indications of partial structural breakdown of the perovskite structure, progressive Cu enrichment renders the structure less stable, and for LCM73, exsolution of Cu particles is clearly observed (Panel F, inset).

### 3.3. Consequences of the Cu-perovskite engineering for catalytic deNOx activity

Activity tests in the NO reduction by CO are shown in Figs. 5 and 6, based on NO conversion and product distribution, respectively. According to the NO conversion results, substitution of 30 % of the Mn sites with Cu (LCM37) increases the catalytic activity over the entire reaction temperature range and shifts the reaction onset temperature to about 50 °C lower temperatures compared to the parent LM perovskite. By further increasing the amount of copper, not only the low-temperature activity of the catalyst does not improve, but also the reaction onset temperature shifts to higher values and in the case of LC, it becomes even worse than the parent LM catalyst. At higher temperatures (>40 % conversion), the conversion trend up to LCM73 follows the copper amount. These results show that there is an optimum value for substitution of Mn by Cu in the perovskite structure. According to the product distribution profiles (Fig. 6), the production sequence of different gas phase species during the reaction is $CO_2$, $N_2O$ and $N_2$, which is qualitatively similar for almost all catalysts. The results show that substituting Mn by Cu also greatly impacts product distribution in such a way that the production of $N_2O$ is limited for the Cu-containing catalysts, and as a result, the production of $N_2$ as a desired product increases significantly. In order to better compare the promotion effects of Cu doping also on product distribution, the $N_2$ selectivity is shown in Fig. S9. By incorporation of copper, the $N_2$ selectivity increases and generally, clear differences between catalysts with different level of Cu doping are evident.

From a mechanistic point of view, the negative NO conversion at low temperatures (50 °C–110 °C, Fig. 5, panel B) and before the onset of $N_2O$ production, which is common to all catalysts, is remarkable. To discuss this mechanistic phenomenon, we have summarized the NO conversion, $N_2O$ and $CO_2$ formation profiles for LCM73-700C in Fig. S10. Also, in order to make the mechanistic pathway easier to understand, a set of elementary reactions, including surface reactions during the prevailing Langmuir-Hinshelwood reaction mechanism (Eqs. (1)-(7)) and also the
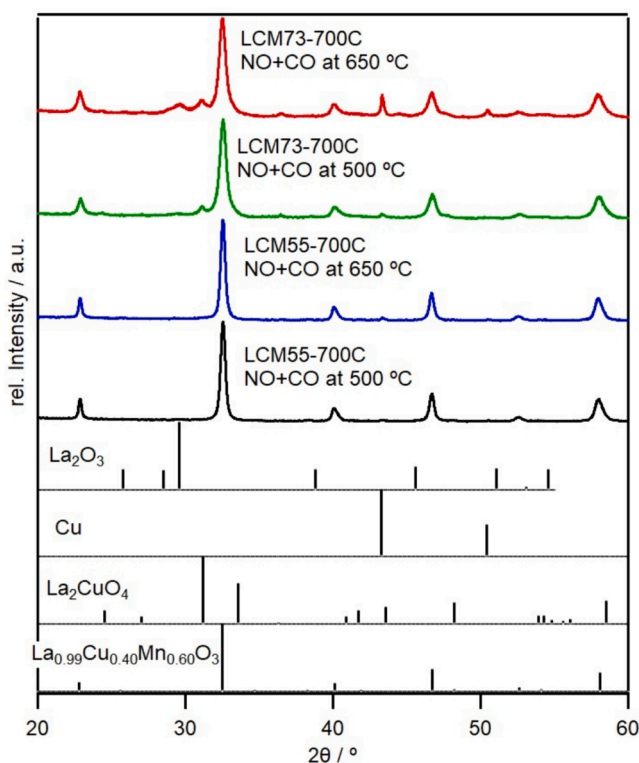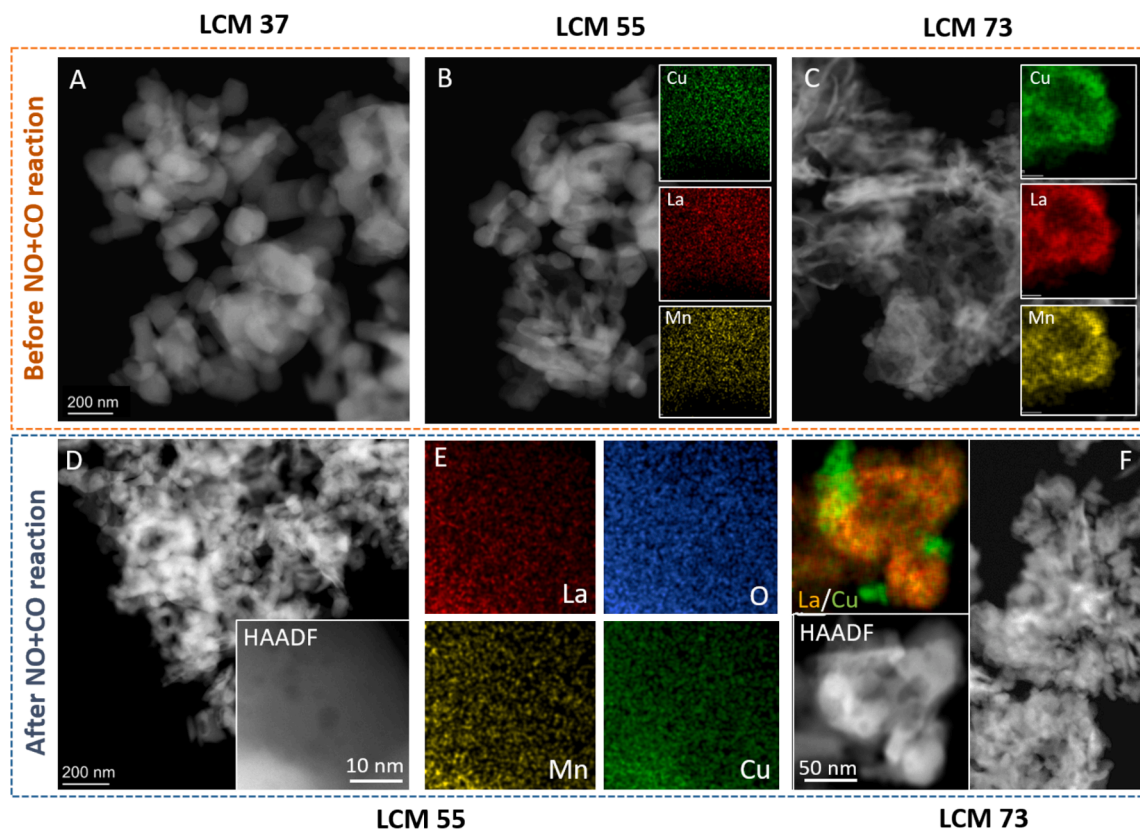
**Fig. 4.** Aberration-corrected electron microscopy images of LCM37, LCM55 and LCM73 after initial calcination at 700 °C (top row, Panels A-C) and for LCM55 and LCM73 after the NO+CO reaction at 500 °C (bottom row, Panels D-E LCM55, Panel F LCM73). EDX maps are shown as inset in Panels B, C, E and F as La-K, Cu-K, Mn-K and O-K intensities. The respective HAADF images are highlighted as insets in Figures D and E.
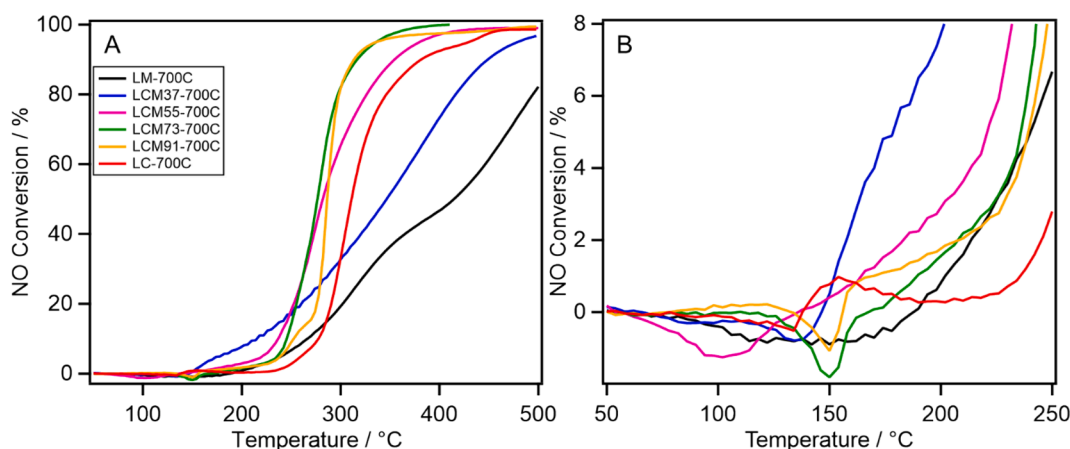


**Fig. 5.** Panel A: NO conversion profiles during the NO reduction by CO for all LCM catalysts calcined at 700 °C. Total gas flow rate: 200 mL min$^{-1}$ with a composition of (CO:NO:He = 1:1:98) of the inlet flow. Heating ramp: 2 °C min$^{-1}$ between 50 °C and 500 °C. Sample mass: 200 mg. Panel B: zoomed NO conversion profiles at low temperatures.

participation of structural oxygen of the catalyst during Mars-van Kre-velen type reaction (Eqs. I and II), are provided in the SI. These elementary reaction steps include reactant adsorption, reaction of intermediates, and product desorption. In each equation, S refers to step-specific catalytically active sites, but not all of them necessarily refer to the same site type and location. According to Fig. S10, the negative NO conversion is accompanied by a relative increase in $CO_2$ production. This behavior is caused by the comparatively strong NO adsorption (compared to CO) on the catalyst surface at low temperatures, which covers the catalyst surface and is also reported for other Mn-based

perovskites [48]. By increasing the temperature, molecular NO (and/or NO$_x$ species) starts to desorb (and/or decompose) again to the gas phase without any reaction, leading to negative NO conversion. The desorption of NO provides vacant catalytic sites for further adsorption and reaction of CO, which leads to a relative increase in the $CO_2$ production rate. In addition, as expected, these results roughly show that the behavior of the catalyst to adsorb reactants is a function of the catalyst composition, as minimum NO conversion occurs at different temperatures for different Cu doping levels.

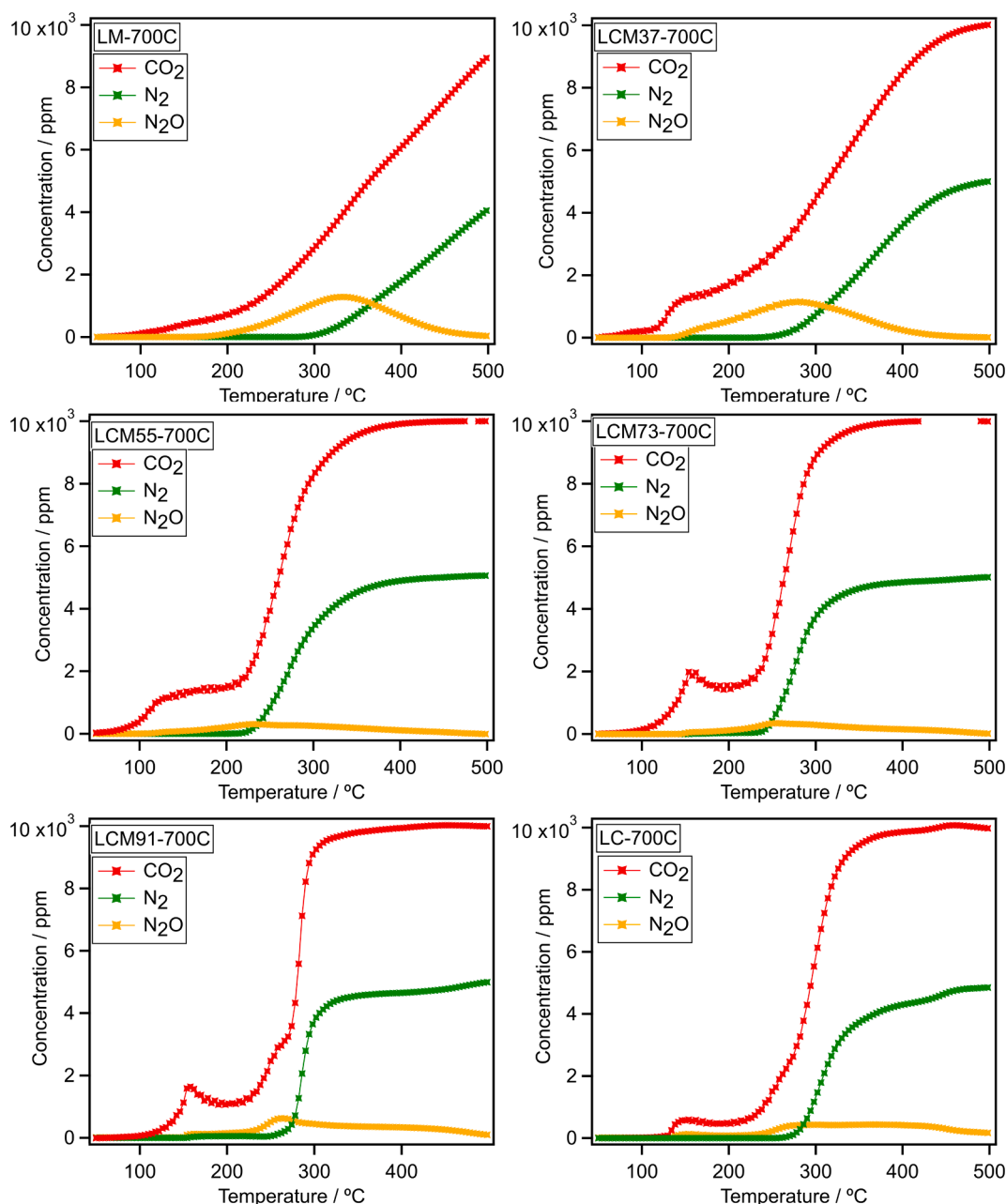Another important point is the production of $CO_2$ at low

**Fig. 6.** Product distribution for all LCM samples during the NO reduction by CO. Total gas flow rate: 200 mL min$^{-1}$ with a composition of (CO:NO:He = 1:1:98) of the inlet flow. Heating ramp: 2 °C min$^{-1}$ between 50 °C and 500 °C. Sample mass: 200 mg.

temperatures and before the production of $N_2O$. As $N_2O$ production is a hint for beginning NO dissociation, the early $CO_2$ production can be explained by a Mars-van Krevelen type reaction mechanism leading to the formation of $CO_2$ using reactive oxygen relased from the crystal structure (Eq. I, in SI). In order to clarify this mechanistic hypothesis experimentally, additional CO-TPR experiments in the flow reactor setup under similar operating conditions to the NO+CO reaction conditions were performed. The only difference between the CO-TPR and NO+CO experiments is that in the case of CO-TPR, NO is excluded from the reaction feed and replaced by an additional flow of He to keep the total flow rate at 200 ml.min$^{-1}$. In Fig. 7, the $CO_2$ formation profile during the CO-TPR reaction is shown in comparison with the formation of $CO_2$ and $N_2O$ during the NO+CO reaction for LCM55-600C and LCM55-700C catalysts as a representative example for all catalysts. Before a significant increase in $N_2O$ concentration during NO+CO reaction (temperature ranges between 50 °C–110 °C) is observed, $CO_2$

formation levels are almost comparable with the $CO_2$ levels during the CO-TPR reaction. This suggests that the reduction of the catalyst and the creation of oxygen vacancies near the surface regions by CO are the first steps in starting the NO+CO reaction [4]. After the partial reduction of NO and the formation of $N_2O$, the level of $CO_2$ formation during the CO-TPR reaction becomes higher than in the NO+CO reaction. According to the elementary reactions in deNO$_x$ reaction system [4,37,49], the partial reduction of NO to $N_2O$ leaves an additional oxygen at the catalyst surface, which is subsequently consumed by CO to form $CO_2$. Therefore, compared to the CO-TPR reaction conditions, the presence of this excess oxygen on the surface under NO+CO reaction conditions changes the chemical potential of oxygen between the surface and the bulk of the catalyst, reducing the oxygen supply rate from the bulk to the surface. However, because the oxygen delivery by the NO dissociation mechanism is still slow due to the low reaction temperature, the balanced final rate is a decrease in the level of $CO_2$ production under NO+CO reaction
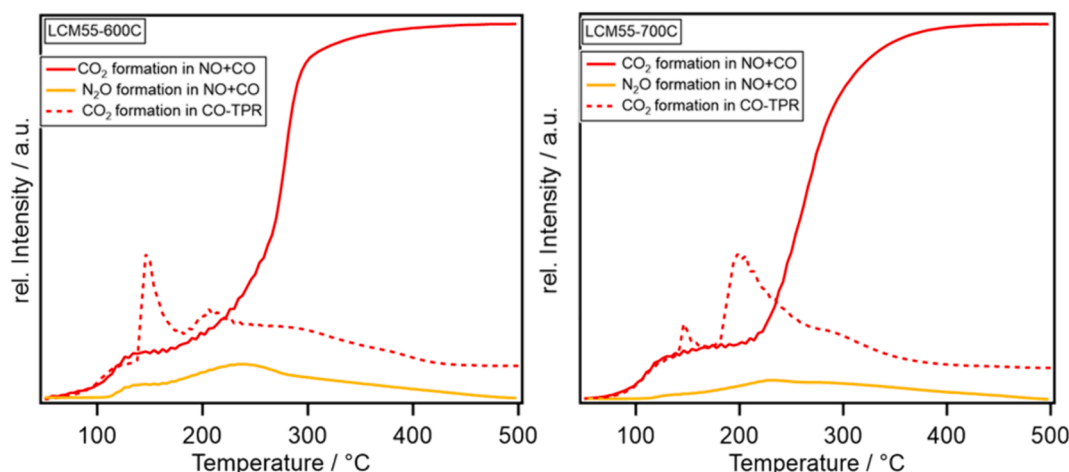
**Fig. 7.** Comparison of the formation of $CO_2$ during CO-TPR reaction with the formation of $CO_2$ and $N_2O$ during the NO+CO reaction on LCM55-600C (left) and LCM55-700C (right). CO-TPR: Total gas flow rate: 200 mL min$^{-1}$ with a composition of (CO:He = 1:99) of the inlet flow. Heating ramp: 2 °C min$^{-1}$ between 50 °C and 500 °C. Sample mass: 200 mg. NO+CO reaction: identical to Fig. 5.

conditions. This observation directly shows that at low temperatures, the NO dissociation is the limiting reaction step. As discussed below, the enhancement of low-temperature activity of catalysts is due to the formation of reduced sites on the catalyst surface.

We also determined the activity of the catalysts during a second cycle as a function of the Cu/Mn ratio and calcination temperature. The catalytic activity of LM-700C during a second cycle is shown in Fig. S11 in comparison to the first cycle after reaction at 650 °C. Although the reaction onset temperature is the same for both catalytic cycles, indicating that the kinetics of the reaction is the same for both, the catalyst loses some of its activity during the second cycle, which most likely could be due to partial sintering and reduction in active sites because of the high reaction temperature.

Fig. 8 shows the catalytic activity and $N_2O$ production trends of LCM37-700C during the first and second cycle, where the maximum reaction temperature is 500 °C. During the second cycle, the NO conversion and $N_2O$ formation onset temperature decreases, and the overall $N_2O$ production level is much lower than during the first cycle, which indicates that the catalyst has become more active for NO dissociation and intermediate $N_2O$ decomposition. As an indirect interpretation, this improvement in catalytic activity and significant improvement in selectivity is due to the partial reduction of the catalyst after the first cycle. As a potentially alternative interpretation, the same feature could be caused by finely dispersed Cu aggregates, which we do not observe in neither TEM nor PXRD.

In addition, the catalytic activity of LCM55-700C and LCM73-700C during the first and second catalytic cycle at two different maximum reaction temperatures of 500 °C and 650 °C are shown in Figs. S12 and

S13, respectively. For both catalysts, for reaction temperatures up to 500 °C, the activity of the catalysts improves kinetically at low temperatures during the second cycle, which is due to the formation of metallic copper particles and the reactivity of the metal-perovskite phase boundary (cf. Figs. 3 and 4). The low activity of both catalysts during the second cycle compared to their first cycle at temperatures above 250 °C indicates that the total number of active sites has decreased compared to the first cycle. From this discussion we conclude that the metal-perovskite phase boundary is also an energetically optimal active site that can catalyze the reaction at low temperatures, and the copper species present in the perovskite structure can also be considered as active sites that are activated at higher temperatures. As discussed in the XPS section and supported by PXRD and TEM, after the reaction and as a result of exsolution, the existence of areas on the surface of the perovskite catalyst with a low concentration of copper can be predicted, which means that its initial dispersion is reduced. Wang et al. [32] found that iron exsolution from STF perovskite generates a highly Fe-deficient near-surface layer of about 2 nm thickness and associated transformations in the crystal structure of the surface, which highlights the changes in oxide surface properties aside from the formation of phase boundary. In addition, the parent bulk perovskite is generally sensitive to sintering, as shown for LM in Fig. S11. When the reaction temperature is increased to 650 °C, the catalyst performs worse in the second cycle than in the first cycle over the entire temperature range. These results, alongside PXRD (Fig. 3), show that the Cu-perovskite phase boundary is diminished due to both growth and agglomeration of copper particles and significant reduction because of high-temperature activity, which cannot improve the reaction kinetics.
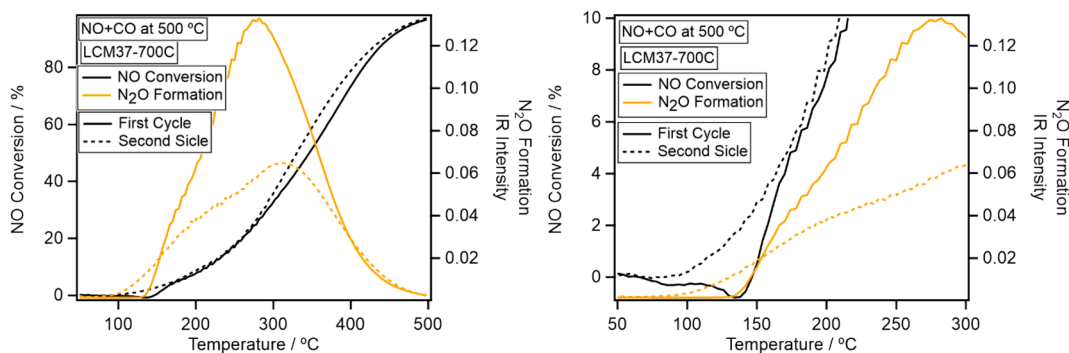


**Fig. 8.** Catalytic activity and $N_2O$ formation profiles on the LCM37-700C catalyst in NO reduction by CO during the first and second catalytic cycle up to 500 °C. Experimental condition: identical to Fig. 5.

Also the direct comparison of the second cycle catalytic results of LCM55-700C and LCM73-700C catalysts after the reaction at 650 °C (Fig. S14) indicates that LCM73-700C features worse NO+CO reaction kinetics than LCM55-700C, strongly suggesting that a large amount of copper contributes to easy sintering of copper particles and the reduction of phase boundary at high reaction temperatures.

Fig. S15 shows the dependence of the catalytic activity of LCM55 on the calcination temperature. Increasing the calcination temperature from 700 °C to 1000 °C, leads to catalyst deactivation, which is evident especially by the shift of the reaction onset temperature to higher temperatures. This is directly related to the increase in crystallite size of the catalyst and the suppression of the primary reduction process by CO, which is a prerequisite to starting the reaction (discussed in detail in the $H_2$/CO TPR section). Furthermore, the improvement in the second cycle catalytic activity of LCM55-1000C at low temperatures after one prior catalytic cycle at 650 °C (Fig. S16) is detectable, but very limited. However, unlike for LCM55-700C and LCM73-700C catalysts, the high-temperature activity during the second cycle matches that during the first cycle. Therefore, when comparing the first and second catalytic cycles, the behavior of the LCM55-1000C appears to be similar to that of the LCM37-700C. Similar to LCM37-700C, PXRD results do not indicate the exsolution of copper particles for LCM55-1000C. Unlike for LCM37-700C, where the stability of copper within the perovskite structure is due to the low copper amount, for LCM55-1000C the stability is essentially due to the high calcination temperature, which can lead to the suppression of perovskite reduction and the subsequent exsolution process. In addition, as the calcination is performed at a very high temperature (1000 °C), at lower reaction temperatures (i.e., 650 °C), bulk perovskite sintering is not anticipated. To prove this assumption and to unlock the reduction/exsolution for LCM55-1000C, we have conducted a NO+CO reaction as a second cycle after a reduction in 1 % CO in flowing He at 650 °C. Fig. S17 clearly shows that kinetic activation of the catalyst due to phase boundary formation occurs, which means that for catalysts that have a suppressed tendency to exsolution, stronger reducing conditions are required for the exsolution to occur.

### 3.4. Influence of the redox properties under $H_2$ and CO reduction conditions on the reactivity of the NO reduction by CO

#### 3.4.1. Reduction profiles in hydrogen

Fig. 9 (left Panel) shows the temperature-programmed $H_2$ reduction profiles for LCM catalysts with different copper amounts calcined at 700 °C. The solid black traces show the integral $H_2$ uptake of the catalysts as a function of temperature during the heating phase of the experiment, and the $H_2$ uptake profiles during the cooling phase of the

$H_2$-TPR are shown as broken lines. To highlight the $H_2$ consumption onset temperatures and peaks during heating, the temperature-dependent first derivative of the integral $H_2$ uptake, i.e., the uptake rate, is additionally shown in Fig. S18. The onset temperature for the major $H_2$ uptake on LM-700C is about 310 °C, the uptake rate peaks at 350 °C and saturates at ~480 °C, suggesting a diffusion-controlled reduction mechanism beyond 500 °C. The reduction process continues isothermally at 700 °C, and it almost ceases during cooling. The onset of the $H_2$ consumption temperature for the Cu-substituted samples is much lower compared to undoped LM, indicating that Cu incorporation into LM considerably improves the $H_2$ activation and reduction kinetics. Although there is no specific trend for the starting temperature of reduction with hydrogen, at least it can be clearly seen that increasing the amount of copper does not correlate directly with a further improvement in activation kinetics (similar to the catalytic activity results). All the Cu-containing perovskites exhibit a first reduction peak around 250 °C. However, increasing the amount of copper quantitatively increases the amount of hydrogen consumption. For example, for LCM55-700C and higher Cu amounts, all hydrogen in the reactor is consumed at a temperature below 400 °C. Therefore, the reduction process, in fact, stops during further heating to 700 °C. This observation also shows that by increasing the amount of copper from LCM37 to LCM55, the reduction is no longer limited by diffusion phenomena. In order to investigate the effect of calcination temperature on hydrogen activation kinetics, $H_2$-TPR results on LCM55-700C, LCM55-850C and LCM55-1000C catalysts are shown in Fig. 9, right Panel. Similar to the catalytic activity results (Fig. S15), as the calcination temperature increases, the reduction activation temperature also increases, indicating that the reduction of the catalyst becomes increasingly difficult. Referring again to the catalytic data, this important result corroborates that partial reduction of the catalyst is necessary for the reaction to start. Although the $H_2$-TPR results can explain some aspects of the catalytic activity trends, the formation of $CO_2$ at low temperatures (as a starting point to reduction of the catalyst during NO+CO), as well as the negative effect of the copper amount on the reaction onset temperature are still in conflict with the $H_2$-TPR results. Therefore, we hypothesize that the observed differences are due to the different kinetic reduction potentials of CO and $H_2$. In order to relate the catalysis results directly to the redox behavior of the catalysts, we tested the activity of the catalysts for CO-TPR.

#### 3.4.2. Reduction profiles in CO

The CO-TPR profiles of the catalysts are shown in Fig. 10, Panels A-D based on $CO_2$ formation and integral $CO_2$ formation, respectively, as a function of copper amount (Panels A and B) and calcination temperature
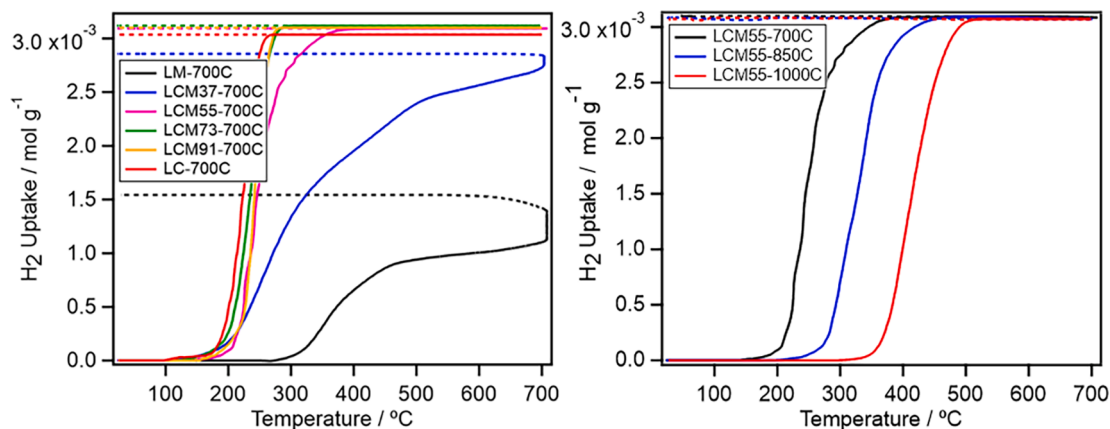


**Fig. 9.** Left: static temperature-programmed $H_2$-reduction on LCM catalysts with different compositions calcined at 700 °C after pre-oxidation in flowing $O_2$ using an initial $H_2$ pressure of 125 mbar. Temperature program: heating from room temperature to 700 °C (10 °C min$^{-1}$/full lines), followed by an isothermal period at the maximum temperature (at 700 °C for 10 min/full line) and a cooling phase (10 °C min$^{-1}$/broken line). The integral $H_2$ uptake (black) is scaled on the left axis. Right: $H_2$-TPR profiles of LCM55 catalysts calcined at different calcination temperatures of 700 °C, 850 °C and 1000 °C.
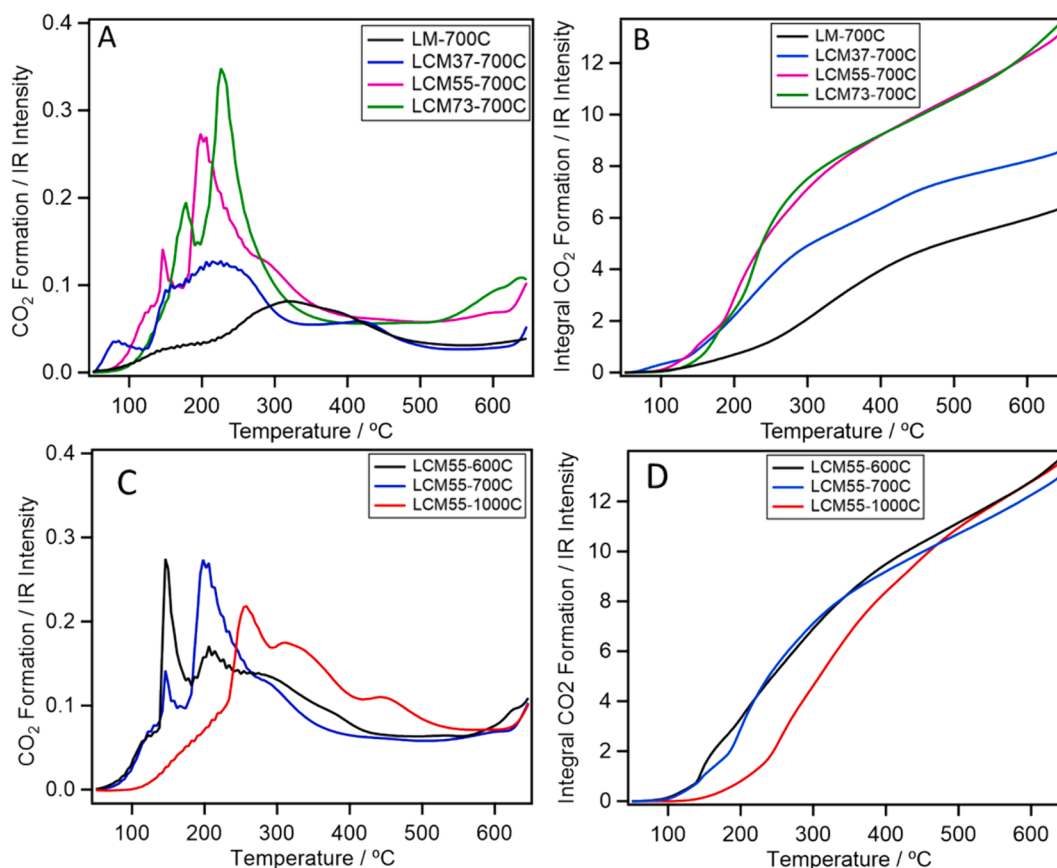
**Fig. 10.** $CO_2$ formation rate (left) and integral (right) profiles in flowing CO-TPR on LCM-based catalysts with different compositions (A and B) and $CO_2$-TPR profiles of LCM55 catalysts calcined at different calcination temperatures of 700 °C, 850 °C and 1000 °C. Operating condition: Total gas flow rate: 200 mL min$^{-1}$ with a composition of (CO:He = 1:99) of the inlet flow. Heating ramp: 2 °C/min between 50 °C and 650 °C. Sample mass: 200 mg.

at a selected Cu/Mn ratio (Panel C and D). In order not to overload the figure, the CO-TPR profiles of LCM91-700C and LC-700C are shown only in Fig. S19. In essence, like in the $H_2$-TPR and catalytic activity tests, we note that incorporation of Cu into the LM perovskite structure up to LCM55 leads to improvement in $CO_2$ formation (i.e., CO consumption) both kinetically and quantitatively. Further increase in Cu content to LCM73-700C has a negative effect on the reduction kinetics. According to Panel B, the integral formation of $CO_2$ for both LCM55-700C and LCM73-700C is almost comparable, which we tentatively assign to partial suppression of reducible sites necessary for reactant activation. In other words, the extra amount of copper in LCM73 is limited to reduction by CO under these experimental conditions. The most important result is that the trends for CO-TPR onset temperature follows the NO+CO reaction trends for each catalyst. Also, the appearance of different distinguishable CO reduction peaks could be due to the presence of different kinetically accessible reduction sites at the surface. This is because the bulk mobility of oxygen during the reduction is not a rate limiting step as shown by the $H_2$-TPR. Therefore, it can be concluded that although the reduction kinetics with CO is improved at low temperature, $H_2$ is a better reducing agent at high temperatures and causes a more thorough reduction of the catalyst. As shown by TEM in our previous work [1,6], one of the reasons for this could be the formation of amorphous carbon covering the active sites in the presence of CO via the Boudouard reaction. Fig. 10 Panels C and D finally show that an increase in calcination temperature for LCM 55 shifts the onset of the reduction temperature to higher temperatures. Nevertheless, the final integral $CO_2$ formation (Panel D) at the maximum temperature is almost similar for all three catalysts.

### 3.4.3. $O_2$-TPD profiles

In addition to CO/$H_2$ TPR experiments, $O_2$-TPD as a measure of catalysts' reducibility and structural oxygen mobility was also performed (Fig. 11). For LM-700C, after a minor, but still detectable $O_2$-desorption ($m/z = 32$) peak at around 170° C, the major $O_2$-desorption starts at around 375° C and accelerates at temperatures higher than 500° C and peaking at around 600 °C. In the case of LCM37-700C, the
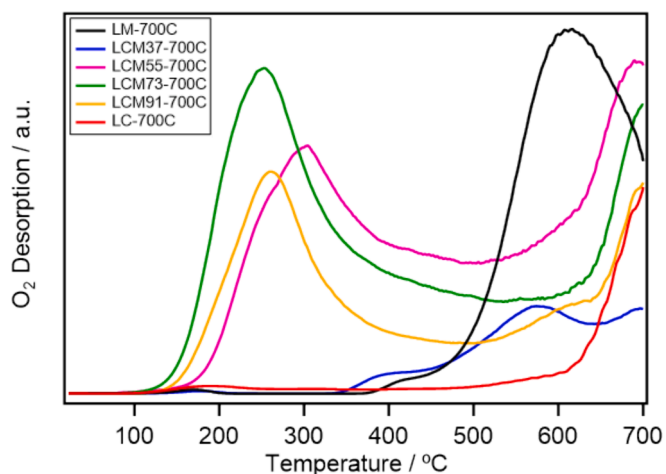


**Fig. 11.** $O_2$-TPD profiles obtained from the LCM samples. All samples were pretreated at 700 °C in flowing dry $O_2$. The base pressure of the system before starting TPD was ca. 9•10$^{-7}$ mbar. Heating ramp: 10 °C/min between 25 °C and 700 °C. Sample mass: 100 mg.

desorption onset temperature shifts to 340° C and up to 470° C, the level of $O_2$ desorption is higher than LM-700 C. Generally, metal oxides contain different types of oxygen species that can be desorbed during the TPD conditions. Based on literature the desorption can be classified into two general forms of (i) α oxygen, mostly referring to surface adsorbed species like $O_2^-/O^-$, desorbing at low temperatures and (ii) β oxygen, which refers to lattice oxygen ($O^{2-}$) and exhibits a relatively high temperature desorption peak [21,50–53]. Considering the strength of oxygen bonding to different cations with different oxidation states and also that the desorption rate of lattice oxygen from the catalyst bulk can be affected by diffusion limitations as compared to the layers near the surface, it is not possible to assign a specific temperature range for the desorption of each of these species. By comparing the desorption profiles of LM and LCM37, it is clear that in LCM37, the oxygen desorption kinetics is improved, however, over the entire TPD temperature range, the integral amount of desorbed oxygen in LM is higher than LCM37. Considering the specific surface area of two catalysts (Table 1), this discrepancy can be answered by the concept of oxygen stoichiometry. Vogel et. al. in turn calculated the oxygen content of these catalysts as $LaMnO_{3.13}$ and $LaMn_{0.7}Cu_{0.3}O_{2.96}$.[54].

By increasing the copper doping level to LCM55 and LCM73 the major desorption temperature decreases by about 200° C. This means that by increasing the doping level of Cu, the amount of reactive oxygen is increased significantly and can be translated to catalytic activity of the catalysts in the NO+CO reaction. Similar to the CO-TPR results, further increasing of the copper level to LCM91 and LC does not improve the oxygen evolution kinetically, as well as quantitively.

*NO-TPD profiles after $O_2$-TPD*.

Fig. 12 shows the NO desorption ($m/z = 30$) profiles of the LCM catalysts after adsorption of NO at RT in comparison to each other. Generally, at least two distinguishable NO desorption peaks starting from almost room temperature were observed for all catalysts. It should be mentioned that small amounts of $N_2O$ ($m/z = 46$) and $N_2$ ($m/z = 28$) which are not shown in this Figure, were detected for all catalysts during NO-TPD. According to the elementary reaction steps (Eqs. (1)-(7) and I/ II, SI) this indicates that the catalysts are active for the dissociation of NO even in the absence of the reducing agent. The formation of $N_2O/N_2$, which indicates the relative effectiveness of the catalysts for $deNO_x$ application is not unexpected, as the catalysts are exposed to $O_2$-TPD before NO absorption. This turns the catalysts into partially reduced states. Activation of NO on oxygen vacancies is a well-known phenomenon and according to Fig. 12, LM-700C exhibits two broad NO
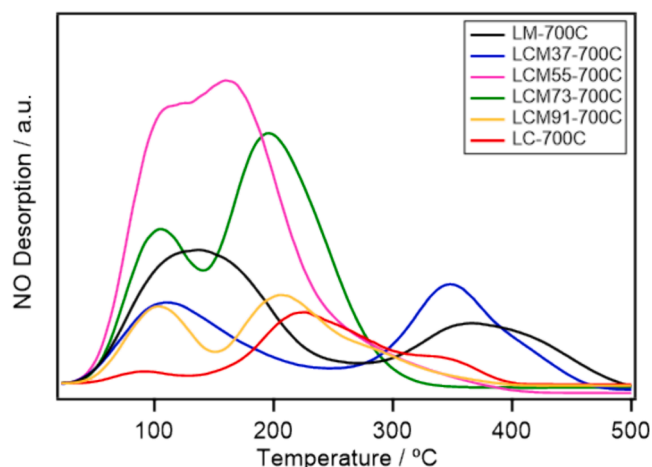


**Fig. 12.** NO-TPD profiles obtained from the LCM samples after adsorption of 1000 mbar dry NO at room temperature (25 °C) for 45 min. All samples were pre-treated at 700 °C during $O_2$-TPD *in vacuo*. The base pressure of the system before starting TPD was ~$9 \cdot 10^{-7}$ mbar. Heating ramp: 10 °C/min between 25 °C and 700 °C. Sample mass: 100 mg.

desorption peaks with maxima around 150° C and 400° C. LCM37-700C also shows two desorption peaks with a slight shift of the maxima of both peaks to lower temperatures. By increasing the Cu-doping level, the difference in the catalysts for NO absorption is much more pronounced, indicating a difference in surface structure of the catalysts. For LCM55-700C and LCM73-700C, the high temperature NO desorption peak is significantly shifted to low temperatures, as well as the amount of adsorbed $NO_x$ is increased. It is worth mentioning, that from the catalytic point of view for $deNO_x$ applications, an increased amount of adsorbed $NO_x$, which can be desorbed/converted at intermediate temperatures, is very important. The thermal stability of the adsorbed NO species again increases by increasing Cu doping level to LCM91-700C and LC-700C.

We also note, that evaluation of the oxygen desorption profiles ($m/z = 32$) together with NO desorption during the NO-TPD experiments (Fig. S20) is illuminating. For the LM-700C and LCM37-700C catalysts, the second NO desorption peak is accompanied by a pronounced $O_2$ desorption peak. This $O_2$ desorption peak can be the result of the desorption/decomposition of adsorbed $NO_x$ species like nitrate and nitrite into NO and $O_2$ [37,55]. $O_2$-desorption peaks at temperatures higher than 500° C (different desorption onset for different catalysts) can also be related to direct $O_2$ desorption from perovskite or copper oxide structures and associated formation of oxygen vacancies. By increasing the amount of copper to LCM55 and higher, the low temperature $O_2$ desorption peak, which is accompanied by the high temperature NO desorption peak, is no longer present. This means that for these catalysts, the oxygen resulting from the decomposition of $NO_x$ species has been captured by the perovskite for quenching of oxygen vacancies or the oxidation of copper species. Considering the elementary reaction steps in the NO+CO environment, this captured oxygen by the catalyst can be used readily for the oxidation of CO. Therefore, it can be concluded that the addition of copper helps the redox cycling during the NO+CO reaction.

In line with the importance of the surface chemistry of the catalysts, the presence and amount of Brønsted and Lewis acidic sites was tested by adsorption of $NH_3$ at room temperature by DRIFT spectroscopy on LM-700C, LCM55-700C and LCM73-700C (Fig. S21). We have provided a detailed discussion in the context of Fig. S21, but in summary, the incorporation of Cu into the perovskite structure introduces very different and complex surface sites compared to LM including formation of potential new sites for the NO+CO reaction.

### 3.4.4. Effect of oxygen on catalytic activity

In order to evaluate the tolerance of the catalysts for oxygen in NO+CO reaction mixture, we studied the reaction also in the presence of different $O_2$ concentrations. According to Fig. S22, in the presence of 4 % $O_2$ (8 times more than the stoichiometry required for the reaction with the reducing agent) LCM55 exhibits a higher rate of $N_2O$ formation during NO+CO+$O_2$ reaction compared to LM and LCM37. Although the conversion levels are very small under these conditions, considering the formation of $N_2O$ as a by-product in partial reduction of $NO_x$, these results indicate that activation of $NO/NO_2$ is more efficient on LCM55. Therefore, LCM55 was chosen for further study. The results for LCM55 as a function of reaction temperature and $O_2$ concentration are shown in Fig. 13, through panels A-D, for $NO_x$ ($NO+NO_2$) conversion, $CO_2$ formation profiles, $N_2O$ concentration and $N_2$ selectivity, respectively. Panel A highlights, that the catalyst can still perform above 90 % $NO_x$ conversion at low $O_2$ concentrations, but loses its activity in $O_2$-richer environments (4 % $O_2$). This behaviour in the presence of $O_2$ is a common feature on different catalysts [56]. According to $N_2O$ production and $N_2$ selectivity profiles (panels C and D), although generally $N_2$ is the main product of $NO_x$ reduction, it is evident that the presence of $O_2$ shifts also the product distribution toward decreasing $N_2$ selectivity. Evaluation of the corresponding $CO_2$ production profiles (Panel B) leads to more mechanistic information on the reaction system. The results show that the onset temperature of $CO_2$ production is the same for all four
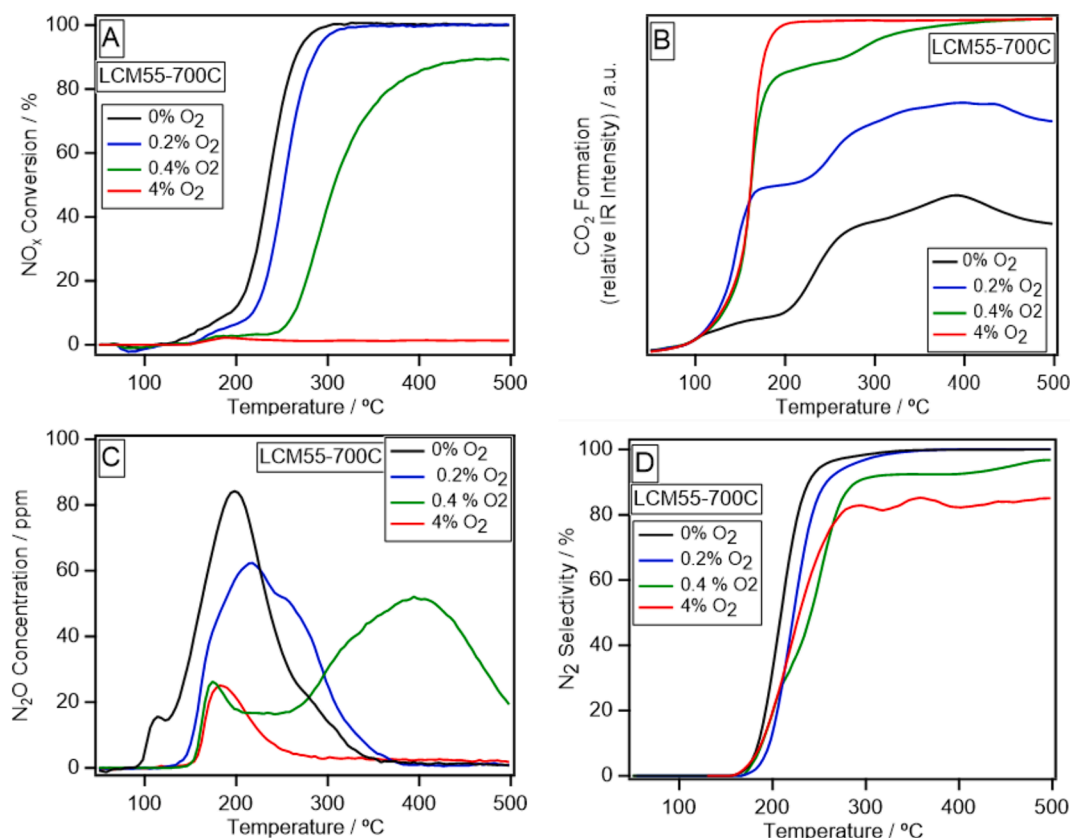
**Fig. 13.** Effect of the $O_2$ concentration on $NO_x$ conversion (Panel A), $CO_2$ formation (Panel B), $N_2O$ concentration (Panel C) and $N_2$ Selectivity (Panel D) of LCM55-700C under 1 % CO+1600 ppm NO and $O_2$ with varied concentration. Other experimental conditions: identical to Fig. 5.

experiments (without presence of $O_2$ and with different $O_2$ concentrations). As discussed in detailed in section 3.3 (Fig. 7) the initial formation of $CO_2$ can be related to CO oxidation using reactive oxygen released from the catalyst structure, which is also valid in the presence of $O_2$. This initiation step of reaction can produce oxygen vacancies as a reactive site for further $O_2$ and NO dissociation and closes the reaction cycle. Another important result an be derived from comparing the onset temperature of $CO_2$ production in the presence and absence of $O_2$ (black and blue curves). They deviate at a temperature of 110 °C–because the onset temperature for $N_2O$ production (as a sign for NO dissociation) in the presence of $O_2$ is higher (~150 °C), the O-species required for $CO_2$ formation under these condition cannot be related to NO dissociation. We rather relate it to $O_2$ dissociation or decomposition of $NO_2$ to NO and O-species, according to the elementary reactions (8)-(13). The higher reaction rate of $O_2$ + CO compared to NO+CO is also reported in ref. [57]. The changes in the production of $CO_2$ at temperatures above 300 °C when $O_2$ (not shown) and NO reach 100 % conversion, are related to the reduction of the catalyst by remaining CO in the reaction mixture as its amount is higher than required by stoichiometry. However, by comparing the $N_2O$ formation in the presence of 4 % $O_2$ and 1 % CO for different NO concentrations of 0.16 % and 1 % (Fig. 13, Panel C and Fig. S22, respectively), we conclude that under these conditions, by increasing the NO partial pressure the possibility of the $N_2O$ reaction increases. This means that the adverse effect of $O_2$ on the NO conversion, in addition to the consumption of reductant, can be related to the occupation of surface-active sites and preventing its adsorption and reaction. It is important to mention here that in the absence of $O_2$, the opposite situation is true and the reaction rate is negative with respect to NO pressure. As shown in the Fig. S23, the NO conversion is improved by reducing its amount from 1.0 % to 0.16 %. As it is also discussed in section 3.3 this behavior can be related to the stronger adsorption of NO compared to CO on catalyst surface.

## 4. Conclusions

By adjusting the doping level and the final calcination temperature during the synthesis of a series of noble metal-free LCM-based perovskites, we highlight that the redox chemistry can be optimally tuned to increase the catalytic activity and selectivity to $N_2$ in the catalytic reduction of NO by CO. A prerequisite is the in-situ formation of an extended metal-perovskite phase boundary. Although the parent LM catalyst is quite stable in terms of reduction under the reaction conditions, introduction of Cu beneficially changes the scenario. The associated improvement of redox properties leading to the reduction of the catalyst in the reaction environment and the according creation of oxygen vacancies improves the reaction kinetics and initiates the NO dissociation. Depending on the calcination temperature, Cu/Mn ratio and the reducing agent, as well as the reaction temperature as parameters for Cu-perovskite interfacial steering, surface reduction can induce partial copper exsolution, agglomeration of exsolved Cu particles and eventual decomposition of the catalyst structure. Although the reduced copper perovskite phase boundary is of course kinetically activated, the presence of Cu in an oxidized form dispersed within the parent perovskite structure can also be activated, albeit at higher energy. We have shown that increasing the amount of initial copper incorporated into the perovskite structure can extend the phase boundary, but exceeding the copper amount can lead to increased sintering of copper particles, deactivating the catalyst in subsequent catalytic cycles. Our results show that increasing the calcination temperature, in addition to the initial sintering of the catalyst and shifting the reaction onset temperature to high temperatures in the first cycle, increases the resistance of the catalyst to reduction. As a consequence, stronger reducing conditions than those provided by the NO+CO reaction are required to form a higher amount of phase boundary-bound active sites. In due course, CO-TPR treatments significantly improve the catalytic activity by triggering

the exsolution process. We have also shown that although CO is a better reductant at low temperatures, its impact is reversed at higher temperatures and, accordingly, much lower than H$_2$. Therefore, neither the bulk supply of oxygen nor the bulk diffusion of copper cations are the limiting steps for exsolution, but rather the surface oxygen exchange with CO. In the presence of NO, oxygen derived from NO dissociation changes the oxygen chemical potential between the catalyst surface and bulk. Therefore, limiting the oxygen mobility from the catalyst bulk is also a limiting factor for exsolution. Entangled with redox chemistry, we have also shown the importance of surface chemical aspects of Cu doping related to the decomposition and desorption of NO$_x$ species. We infer that after CO reduction of the surface, the so-created oxygen vacany sites act as active sites for NO adsorption and dissociation. This is is clearly beneficially influenced by the introduction of copper into the perovskite structure. We have also revealed the response of different Cu-perovskite interfaces to the presence of oxygen in the NO+CO reaction mixture. Although we have shown this interplay between redox chemistry and surface-chemical aspects only for copper-containing perovskites as a representative example, we emphasize that the metal-perovskite interface as a result of metal exsolution from perovskites is the key point of catalytic activity and selectivity. Knowledge-based metal-peroskite interfacial engineering by adjusting internal and external structural and reaction parameters is as such inevitable for meaningful catalyst development.

## CRediT authorship contribution statement

**Asghar Mohammadi:** Writing – original draft, Formal analysis, Data curation, Conceptualization. **Clivia Hejny:** Investigation, Formal analysis, Data curation. **Volker Kahlenberg:** Supervision, Formal analysis. **Josef M. Gallmetzer:** Writing – original draft, Formal analysis, Data curation. **Felix R.S. Purtscher:** Formal analysis, Data curation. **Thomas S. Hofer:** Supervision, Formal analysis, Conceptualization. **Marc Heggen:** Formal analysis, Data curation. **Maged F. Bekheet:** Formal analysis, Data curation. **Simon Penner:** Writing – review & editing, Validation, Supervision, Project administration, Funding acquisition, Conceptualization.

## Declaration of competing interest

The authors declare that they have no known competing financial interests or personal relationships that could have appeared to influence the work reported in this paper.

## Data availability

Data will be made available on request.

## Appendix A. Supplementary data

Supplementary data to this article can be found online at https://doi.org/10.1016/j.cej.2024.155425.

## References

[1] R. Di Monte, J. Kaspar, P. Fornasiero, M. Graziani, C. Paze, G. Gubitosa, NO reduction by CO over Pd/Ce0. 6Zr0. 4O2 Al2O3 catalysts: in situ FT-IR studies of NO and CO adsorption, Inorg. Chim. Acta 334 (2002) 318–326.

[2] R.L. Thompson, L. Lassaletta, P.K. Patra, C. Wilson, K.C. Wells, A. Gressent, E. N. Koffi, M.P. Chipperfield, W. Winiwarter, E.A. Davidson, Acceleration of global N2O emissions seen from two decades of atmospheric inversion, Nat. Clim. Chang. 9 (2019) 993–998.

[3] A. Ravishankara, J.S. Daniel, R.W. Portmann, Nitrous oxide (N2O): the dominant ozone-depleting substance emitted in the 21st century, science, 326 (2009) 123–125.

[4] A. Mohammadi, C.W. Thurner, L. Haug, M.F. Bekheet, J.T. Müller, A. Gurlo, C. Hejny, P.D.K. Nezhad, D. Winkler, W. Riedel, How defects in lanthanum iron manganite perovskite structures promote the catalytic reduction of NO by CO, Mater. Today Chem. 35 (2024) 101910.

[5] C.K. Lambert, Current state of the art and future needs for automotive exhaust catalysis, Nat. Catal. 2 (2019) 554–557.

[6] S. Rood, S. Eslava, A. Manigrasso, C. Bannister, Recent advances in gasoline three-way catalyst formulation: a review Proceedings of the Institution of Mechanical Engineers, Part d: J. Automob. Eng. 234 (2020) 936–949.

[7] S. Roy, M. Hegde, G. Madras, Catalysis for NOx abatement, Appl. Energy 86 (2009) 2283–2297.

[8] R. Zhang, A. Villanueva, H. Alamdari, S. Kaliaguine, Reduction of NO by CO over nanoscale LaCo1− xCuxO3 and LaMn1− xCuxO3 perovskites, J. Mol. Catal. A Chem. 258 (2006) 22–34.

[9] S. Peter, E. Garbowski, V. Perrichon, M. Primet, NO reduction by CO over aluminate-supported perovskites, Catal. Lett. 70 (2000) 27–33.

[10] Y. Wu, G. Li, B. Chu, L. Dong, Z. Tong, H. He, L. Zhang, M. Fan, B. Li, L. Dong, NO reduction by CO over highly active and stable perovskite oxide catalysts La0. 8Ce0. 2M0. 25Co0. 75O3 (M= Cu, Mn, Fe): effect of the role in B site, Industrial & Engineering Chemistry Research, 57 (2018) 15670-15682.

[11] R. De Lima, M. Batista, M. Wallau, E. Sanches, Y.P. Mascarenhas, E.A. Urquieta-González, High specific surface area LaFeCo perovskites—Synthesis by nanocasting and catalytic behavior in the reduction of NO with CO, Appl Catal B 90 (2009) 441–450.

[12] J. Hwang, R.R. Rao, L. Giordano, K. Akkiraju, X.R. Wang, E.J. Crumlin, H. Bluhm, Y. Shao-Horn, Regulating oxygen activity of perovskites to promote NO x oxidation and reduction kinetics, Nat. Catal. 4 (2021) 663–673.

[13] X. Zhu, K. Li, L. Neal, F. Li, Perovskites as geo-inspired oxygen storage materials for chemical looping and three-way catalysis: a perspective, ACS Catal. 8 (2018) 8213–8236.

[14] B. Li, M.B. Katz, Y. Duan, X. Du, K. Zhang, L. Chen, A. Van der Ven, G.W. Graham, X. Pan, A joint theoretical and experimental study of phase equilibria and evolution in Pt-doped calcium titanate under redox conditions, Chem. Mater. 27 (2015) 18–28.

[15] N. Li, A. Boréave, J.-P. Deloume, F. Gaillard, Catalytic combustion of toluene over a Sr and Fe substituted LaCoO3 perovskite, Solid State Ion. 179 (2008) 1396–1400.

[16] M.A. Peña, J. Fierro, Chemical structures and performance of perovskite oxides, Chem. Rev. 101 (2001) 1981–2018.

[17] J. Evans, M. Wainwright, A. Bridgewater, D. Young, On the determination of copper surface area by reaction with nitrous oxide, Appl. Catal. 7 (1983) 75–83.

[18] J. Scholten, J. Konvalinka, Reaction of nitrous oxide with copper surfaces Application to the Determination of Free-Copper Surface Areas, Trans. Faraday Soc. 65 (1969) 2465–2473.

[19] A. Tarjomannejad, A. Niaei, A. Farzi, D. Salari, P.R. Zonouz, Catalytic Oxidation of CO Over LaMn 1–x B x O 3 (B= Cu, Fe) Perovskite-type Oxides, Catal. Lett. 146 (2016) 1544–1551.

[20] C.W. Thurner, X. Drexler, L. Haug, D. Winkler, J. Kunze-Liebhäuser, J. Bernardi, B. Klötzer, S. Penner, When copper is not enough: advantages and drawbacks of using copper in de-NOx reactions over lanthanum manganite perovskite structures, Appl Catal B 331 (2023) 122693.

[21] R. Zhang, A. Villanueva, H. Alamdari, S. Kaliaguine, Catalytic reduction of NO by propene over LaCo1− xCuxO3 perovskites synthesized by reactive grinding, Appl Catal B 64 (2006) 220–233.

[22] R. Zhang, A. Villanueva, H. Alamdari, S. Kaliaguine, Cu-and Pd-substituted nanoscale Fe-based perovskites for selective catalytic reduction of NO by propene, J. Catal. 237 (2006) 368–380.

[23] Y. Nishihata, J. Mizuki, T. Akao, H. Tanaka, M. Uenishi, M. Kimura, T. Okamoto, N. Hamada, Self-regeneration of a Pd-perovskite catalyst for automotive emissions control, Nature 418 (2002) 164–167.

[24] Y. Nishihata, J. Mizuki, H. Tanaka, M. Uenishi, M. Kimura, Self-regeneration of palladium-perovskite catalysts in modern automobiles, J. Phys. Chem. Solid 66 (2005) 274–282.

[25] B. Zheng, T. Gan, S. Shi, J. Wang, W. Zhang, X. Zhou, Y. Zou, W. Yan, G. Liu, Exsolution of iron oxide on LaFeO3 perovskite: a robust heterostructured support for constructing self-Adjustable Pt-based room-temperature CO oxidation catalysts, ACS Appl. Mater. Interfaces 13 (2021) 27029–27040.

[26] J. Wang, D. Kalaev, J. Yang, I. Waluyo, A. Hunt, J.T. Sadowski, H.L. Tuller, B. Yildiz, Fast surface oxygen release kinetics accelerate nanoparticle exsolution in perovskite oxides, J. Am. Chem. Soc. 145 (2023) 1714–1727.

[27] D. Neagu, G. Tsekouras, D.N. Miller, H. Ménard, J.T. Irvine, In situ growth of nanoparticles through control of non-stoichiometry, Nat. Chem. 5 (2013) 916–923.

[28] D. Neagu, T.-S. Oh, D.N. Miller, H. Ménard, S.M. Bukhari, S.R. Gamble, R.J. Gorte, J.M. Vohs, J.T. Irvine, Nano-socketed nickel particles with enhanced coking resistance grown in situ by redox exsolution, Nat. Commun. 6 (2015) 8120.

[29] D. Neagu, V. Kyriakou, I.-L. Roiban, M. Aouine, C. Tang, A. Caravaca, K. Kousi, I. Schreur-Piet, I.S. Metcalfe, P. Vernoux, In situ observation of nanoparticle exsolution from perovskite oxides: from atomic scale mechanistic insight to nanostructure tailoring, ACS Nano 13 (2019) 12996–13005.

[30] S. Yu, D. Yoon, Y. Lee, H. Yoon, H. Han, N. Kim, C.-J. Kim, K. Ihm, T.-S. Oh, J. Son, Metal nanoparticle exsolution on a perovskite stannate support with high electrical conductivity, Nano Lett. 20 (2020) 3538–3544.

[31] C.W. Thurner, N. Bonmassar, D. Winkler, L. Haug, K. Ploner, P. Delir Kheyrollahi Nezhad, X. Drexler, A. Mohammadi, P.A. van Aken, J. Kunze-Liebhäuser, Who Does the Job? How Copper Can Replace Noble Metals in Sustainable Catalysis by the Formation of Copper–Mixed Oxide Interfaces, ACS catalysis, 12 (2022) 7696-7708.

[32] J. Wang, A. Kumar, J.L. Wardini, Z. Zhang, H. Zhou, E.J. Crumlin, J.T. Sadowski, K. B. Woller, W.J. Bowman, J.M. LeBeau, Exsolution-driven surface transformation in the host oxide, Nano Lett. 22 (2022) 5401–5408.

[33] K.S. Roy, C. Subramaniam, L.S. Panchakarla, Non-stoichiometry induced exsolution of metal oxide nanoparticles via formation of wavy surfaces and their enhanced electrocatalytic activity: case of misfit calcium cobalt oxide, ACS Appl. Mater. Interfaces 13 (2021) 9897–9907.

[34] U.G. Singh, J. Li, J.W. Bennett, A.M. Rappe, R. Seshadri, S.L. Scott, A Pd-doped perovskite catalyst, BaCe1− xPdxO3− δ, for CO oxidation, J. Catal. 249 (2007) 349–358.

[35] A.K. Opitz, A. Nenning, C. Rameshan, M. Kubicek, T. Götsch, R. Blume, M. Hävecker, A. Knop-Gericke, G.n. Rupprechter, B. Klötzer, Surface chemistry of perovskite-type electrodes during high temperature CO2 electrolysis investigated by operando photoelectron spectroscopy, ACS Appl. Mater. Interfaces 9 (2017) 35847–35860.

[36] J. Li, U.G. Singh, T.D. Schladt, J.K. Stalick, S.L. Scott, R. Seshadri, Hexagonal YFe1− x Pd x O3− δ: nonperovskite host compounds for Pd2+ and their catalytic activity for CO oxidation, Chem. Mater. 20 (2008) 6567–6576.

[37] A. Mohammadi, A. Farzi, C. Thurner, B. Klötzer, S. Schwarz, J. Bernardi, A. Niaei, S. Penner, Tailoring the metal-perovskite interface for promotional steering of the catalytic NO reduction by CO in the presence of H2O on Pd-lanthanum iron manganite composites, Appl Catal B 307 (2022) 121160.

[38] M. Grünbacher, E.-M. Köck, M. Kogler, B. Klötzer, S. Penner, Evidence for dissolved hydrogen in the mixed ionic–electronic conducting perovskites La 0.6 Sr 0.4 FeO 3− δ and SrTi 0.7 Fe 0.3 O 3− δ, PCCP 18 (2016) 26873–26884.

[39] A. Erba, J.K. Desmarais, S. Casassa, B. Civalleri, L. Donà, I.J. Bush, B. Searle, L. Maschio, L. Edith-Daga, A. Cossard, CRYSTAL23: a program for computational solid state physics and chemistry, J. Chem. Theory Comput. (2022).

[40] L. Schimka, J. Harl, G. Kresse, Improved hybrid functional for solids: the HSEsol functional, J. Chem. Phys. 134 (2011).

[41] D. Vilela Oliveira, J. Laun, M.F. Peintinger, T. Bredow, BSSE-correction scheme for consistent gaussian basis sets of double-and triple-zeta valence with polarization quality for solid-state calculations, J. Comput. Chem. 40 (2019) 2364–2376.

[42] F. Izumi, K. Momma, Three-dimensional visualization in powder diffraction, Solid State Phenom. 130 (2007) 15–20.

[43] K. Momma, F. Izumi, VESTA 3 for three-dimensional visualization of crystal, volumetric and morphology data, J. Appl. Cryst. 44 (2011) 1272–1276.

[44] A.N. Petrov, A.Y. Zuev, I. Tikchonova, V.I. Voronin, Crystal and defect structure of the mixed oxides LaMn1− zCuzO3±y (0≤ z≤ 0.4), Solid State Ion. 129 (2000) 179–188.

[45] E. Rini, M.K. Gupta, R. Mittal, A. Mekki, M.H. Al Saeed, S. Sen, Structural change from Pbnm to R3̄c phase with varying Fe/Mn content in (1–x) LaFeO3. xLaMnO3 solid solution leading to modifications in octahedral tilt and valence states, J. Alloy. Compd. 883 (2021) 160761.

[46] W.S. Kim, G. Anoop, H.J. Lee, S.S. Lee, J.H. Kwak, H.J. Lee, J.Y. Jo, Facile synthesis of perovskite LaMnO3+ δ nanoparticles for the oxygen reduction reaction, J. Catal. 344 (2016) 578–582.

[47] W.Y. Jung, K.T. Lim, G.D. Lee, M.S. Lee, S.-S. Hong, Catalytic combustion of benzene over nanosized LaMnO3 perovskite oxides, J. Nanosci. Nanotechnol. 13 (2013) 6120–6124.

[48] J. Tascon, L.G. Tejuca, C.H. Rochester, Surface interactions of NO and CO with LaMO3 oxides, J. Catal. 95 (1985) 558–566.

[49] M. Grünbacher, A. Tarjomannejad, P.D.K. Nezhad, C. Praty, K. Ploner, A. Mohammadi, A. Niaei, B. Klötzer, S. Schwarz, J. Bernardi, Promotion of La (Cu0. 7Mn0. 3) 0.98 M0. 02O3− δ (M= Pd, Pt, Ru and Rh) perovskite catalysts by noble metals for the reduction of NO by CO, Journal of Catalysis, 379 (2019) 18-32.

[50] Q.N. Tran, Green chemistry on perovskite oxide catalysts. Materials Chemistry. Montpellier. Ecole nationale supérieure de chimie; Politecnico di Torino, 2019. English. ⟨NNT : 2019ENCM0011⟩. ⟨tel-03623512⟩.

[51] J. Zhang, X. Weng, Z. Wu, Y. Liu, H. Wang, Facile synthesis of highly active LaCoO3/MgO composite perovskite via simultaneous co-precipitation in supercritical water, Appl Catal B 126 (2012) 231–238.

[52] B. Levasseur, S. Kaliaguine, Methanol oxidation on LaBO3 (B= Co, Mn, Fe) perovskite-type catalysts prepared by reactive grinding, Appl. Catal. A 343 (2008) 29–38.

[53] R. Pereñíguez, J. Hueso, F. Gaillard, J. Holgado, A. Caballero, Study of oxygen reactivity in La 1–x Sr x CoO 3− δ perovskites for total oxidation of toluene, Catal. Lett. 142 (2012) 408–416.

[54] E. Vogel, P. Johnson Jr, P. Gallagher, Oxygen Stoichiometry in LaMn1-xCuxO3+ y by Thermogravimetry, J. Am. Ceram. Soc. 60 (1977) 31–33.

[55] Z. Say, M. Dogac, E.I. Vovk, Y.E. Kalay, C.H. Kim, W. Li, E. Ozensoy, Palladium doped perovskite-based NO oxidation catalysts: the role of Pd and B-sites for NOx adsorption behavior via in-situ spectroscopy, Appl Catal B 154 (2014) 51–61.

[56] Y. Bai, X. Zong, C. Jin, S. Wang, S. Wang, Synergy of single-atom Fe1 and Ce–Ov sites on mesoporous CeO2–Al2O3 for efficient selective catalytic reduction of NO with CO, ACS Catal. 14 (2024) 827–836.

[57] D. Wickham, B. Koel, Steady-state kinetics of the catalytic reduction of nitrogen dioxide by carbon monoxide on platinum, J. Catal. 114 (1988) 207–216.